

Using Green's Functions to Calibrate an Ocean General Circulation Model

DIMITRIS MENEMENLIS, ICHIRO FUKUMORI, AND TONG LEE

Jet Propulsion Laboratory, California Institute of Technology, Pasadena, California

(Manuscript received 29 June 2004, in final form 27 September 2004)

ABSTRACT

Green's functions provide a simple yet effective method to test and to calibrate general circulation model (GCM) parameterizations, to study and to quantify model and data errors, to correct model biases and trends, and to blend estimates from different solutions and data products. The method is applied to an ocean GCM, resulting in substantial improvements of the solution relative to observations when compared to prior estimates: overall model bias and drift are reduced and there is a 10%–30% increase in explained variance. Within the context of this optimization, the following new estimates for commonly used ocean GCM parameters are obtained. Background vertical diffusivity is $(15.1 \pm 0.1) \times 10^{-6} \text{ m}^2 \text{ s}^{-2}$. Background vertical viscosity is $(18 \pm 3) \times 10^{-6} \text{ m}^2 \text{ s}^{-2}$. The critical bulk Richardson number, which sets boundary layer depth, is $Ri_c = 0.354 \pm 0.004$. The threshold gradient Richardson number for shear instability vertical mixing is $Ri_0 = 0.699 \pm 0.008$. The estimated isopycnal diffusivity coefficient ranges from 550 to $1350 \text{ m}^2 \text{ s}^{-2}$, with the largest values occurring at depth in regions of increased mesoscale eddy activity. Surprisingly, the estimated isopycnal diffusivity exhibits a 5%–35% decrease near the surface. Improved estimates of initial and boundary conditions are also obtained. The above estimates are the backbone of a quasi-operational, global-ocean circulation analysis system.

1. Introduction

General circulation models (GCMs) resolve only a minute fraction of the climate-system degrees of freedom (e.g., Holloway 1999). Subgrid-scale processes, which are not resolved by these models, must therefore be represented using statistical or empirical parameterizations. The discussion herein concerns a method, based on the computation of model Green's functions, for calibrating these parameterizations. For illustration purposes, the method is applied to an ocean GCM within the context of a global-ocean data assimilation project.

Example subgrid-scale parameterizations in ocean GCMs are those used to represent the role of eddies, internal waves, small-scale turbulence, etc. For the specific application example discussed here, these processes have been represented using the isopycnal mixing schemes of Redi (1982) and Gent and McWilliams (1990) and the vertical mixing scheme of Large et al. (1994). These schemes contain empirical “diffusion” coefficients, critical Richardson numbers, etc., whose careful calibration is key to obtaining a realistic representation of the physical processes that have been parameterized.

The conventional approach for calibrating empirical parameterizations is to adjust one parameter at a time using GCM sensitivity studies and comparisons with data. But this approach is suboptimal because estimates of these empirical parameters depend on each other and on model configuration, initial conditions, surface boundary conditions, etc. Therefore an optimal set of parameters can only be obtained through the simultaneous adjustment of all of these conditions, a daunting task.

A recent study by Stammer et al. (2003) demonstrates that, using the adjoint method, it is possible to simultaneously adjust the initial and surface boundary conditions of an ocean GCM in order to fit a wide variety of data products. The above study is being extended to include the estimation of the GCM's mixing coefficients (D. Stammer 2003, personal communication). Powerful though it is, the adjoint method does have some drawbacks: it is computationally expensive, its implementation is technically demanding, and it does not easily accommodate error analysis and chaotic systems.

The Green's function approach discussed here provides a different set of trade-offs between optimality, computational cost, error description, and ease of implementation. Key advantages relative to the adjoint method are 1) simplicity of implementation, 2) the possibility of obtaining complete a posteriori error statistics for the parameters being estimated, and 3) im-

Corresponding author address: D. Menemenlis, Jet Propulsion Laboratory, California Institute of Technology, Mail Stop 300–323, 4800 Oak Grove Drive, Pasadena, CA 91109.
E-mail: menemenlis@jpl.nasa.gov

proved robustness in the presence of nonlinearities. The major drawback of the Green's function approach is that computational cost increases linearly with the number of control parameters. By comparison, the cost of the adjoint method, while substantial, is largely independent from the number of control parameters. More will be said later about these various trade-offs.

Green's functions were first used to solve partial differential equations describing electrical, magnetic, mechanical, and thermal phenomena (Challis and Sheard 2003). Green's functions have also been used to linearize and to solve a wide variety of geophysical inverse problems (e.g., Fan et al. 1999; Gloor et al. 2001; Gray and Haine 2001; Wunsch 1996; and references therein). Application examples that are closely related to the present discussion are those of Stammer and Wunsch (1996) and Menemenlis and Wunsch (1997), in which model Green's functions were used to estimate the large-scale Pacific Ocean circulation. What sets apart the present discussion from the work of Stammer and Wunsch (1996) and Menemenlis and Wunsch (1997) is the choice of control parameters. Specifically, model Green's functions are here used to blend existing estimates of initial and surface boundary conditions and to estimate diffusion coefficients, critical Richardson numbers, and relaxation time scales.

The Green's function approach is described in section 2 using, where possible, the notation of Ide et al. (1997). The power of this approach is best illustrated by example. For this purpose sections 3–5 discuss the application of the Green's function approach to improving the estimates of a quasi-operational, global-ocean circulation analysis system. Summary and concluding remarks follow in section 6.

2. Green's function approach

In practice, the Green's function approach involves the computation of GCM sensitivity experiments followed by a recipe for constructing a solution that is the best linear combination of these sensitivity experiments. Technically, Green's functions are used to linearize the GCM, and discrete inverse theory is used to estimate uncertain GCM parameters. The following discussion assumes that the reader is familiar with discrete inverse theory and its application to geophysical data analysis. If not, a brief but excellent introduction is found in Menke (1989).

Algebraically, a GCM can be represented by a set of rules for time stepping a state vector:

$$\mathbf{x}^f(t_{i+1}) = M_i[\mathbf{x}^f(t_i)]. \quad (1)$$

For the ocean GCM example, state vector $\mathbf{x}^f(t_i)$ includes temperature, salinity, velocity, and sea surface height on a predefined grid at discrete time t_i . Function M_i represents the known GCM time-stepping rules, in-

cluding initial conditions, boundary conditions, empirical mixing coefficients, etc.

The discretized dynamics of the true geofluid \mathbf{x}^t are assumed to differ from that of the numerical model (1) by a vector of stochastic perturbations:

$$\mathbf{x}^t(t_{i+1}) = M_i[\mathbf{x}^t(t_i), \boldsymbol{\eta}], \quad (2)$$

where $\boldsymbol{\eta}$ is a noise process, which is assumed to have zero mean and covariance matrix \mathbf{Q} . Vector $\boldsymbol{\eta}$ contains a set of uncertain parameters that can be used as "controls" for bringing the GCM simulation closer to observations. For the ocean GCM example, vector $\boldsymbol{\eta}$ includes terms that represent errors in the initial and boundary conditions and in the empirical mixing coefficients.

The state estimation problem aims to estimate parameters $\boldsymbol{\eta}$ given a set of observations

$$\mathbf{y}^o = H \begin{bmatrix} \mathbf{x}^t(t_0) \\ \vdots \\ \mathbf{x}^t(t_N) \end{bmatrix} + \boldsymbol{\varepsilon}, \quad (3)$$

where vector \mathbf{y}^o represents all available observations during the estimation period, $t_0 \leq t_i \leq t_N$, H is the measurement function, and residual $\boldsymbol{\varepsilon}$ is a noise process, which is assumed to have zero mean and covariance matrix \mathbf{R} . Vector $\boldsymbol{\varepsilon}$ represents measurement errors and all model errors that are not represented by $\boldsymbol{\eta}$ in (2). For the ocean GCM example, $\boldsymbol{\varepsilon}$ includes variability due to internal waves, mesoscale eddies, tides, etc.

For the Green's function approach, Eqs. (2) and (3) are combined, resulting in

$$\mathbf{y}^o = G(\boldsymbol{\eta}) + \boldsymbol{\varepsilon}, \quad (4)$$

where G is the convolution of measurement function H with GCM dynamics M_i . Control parameters $\boldsymbol{\eta}$ can be estimated by minimizing a quadratic cost function

$$J = \boldsymbol{\eta}^T \mathbf{Q}^{-1} \boldsymbol{\eta} + \boldsymbol{\varepsilon}^T \mathbf{R}^{-1} \boldsymbol{\varepsilon}, \quad (5)$$

where superscript T is the transpose operator. Equations (4) and (5) are those of the familiar least squares minimization problem. Complications arise because the dimensions of $\boldsymbol{\eta}$ and of $\boldsymbol{\varepsilon}$ can be huge, because covariance matrices \mathbf{Q} and \mathbf{R} are usually not known, and because function G is nonlinear. Most practical estimation methods assume that (4) can be usefully linearized about a particular GCM trajectory. If the linearization assumption holds, (4) simplifies to

$$\mathbf{y}^d = \mathbf{y}^o - G(\mathbf{0}) = \mathbf{G}\boldsymbol{\eta} + \boldsymbol{\varepsilon}, \quad (6)$$

where $\mathbf{0}$ is the null vector, $G(\mathbf{0})$ is the baseline GCM integration sampled at the data locations, vector \mathbf{y}^d is the model-data difference, and \mathbf{G} is a matrix whose columns are the Green's functions of G . Specifically, the j th column of matrix \mathbf{G} is

$$\mathbf{g}_{(j)} = \frac{G(\mathbf{e}_j) - G(\mathbf{0})}{e_j}, \quad (7)$$

where \mathbf{e}_j is a perturbation vector that is everywhere zero except for element j , which is set to e_j . That is, each column of \mathbf{G} can be computed using a GCM sensitivity experiment. Matrix \mathbf{G} is called the data kernel because it relates the data \mathbf{y}^d with model parameters $\boldsymbol{\eta}$. The minimization of (5) given (6) is a discrete linear inverse problem with solution

$$\boldsymbol{\eta}^a = \mathbf{P}\mathbf{G}^T\mathbf{R}^{-1}\mathbf{y}^d \quad (8)$$

and uncertainty covariance matrix

$$\mathbf{P} = (\mathbf{Q}^{-1} + \mathbf{G}^T\mathbf{R}^{-1}\mathbf{G})^{-1}. \quad (9)$$

Discrete linear inverse theory is the subject of a vast literature, and many useful tools exist for deriving and for analyzing the solutions (e.g., Menke 1989; Wunsch 1996; and references therein).

The validity of the GCM linearization can be tested a posteriori by comparing the residual of Eqs. (4) and (6) for $\boldsymbol{\eta} = \boldsymbol{\eta}^a$. If the linearity assumption holds, then it is expected that $G(\boldsymbol{\eta}^a) - G(\mathbf{0}) \sim \mathbf{G}\boldsymbol{\eta}^a$. Therefore a reasonable requirement is that

$$\text{abs}[G(\boldsymbol{\eta}^a) - G(\mathbf{0}) - \mathbf{G}\boldsymbol{\eta}^a] \ll \text{diag}(\mathbf{R}^{1/2}), \quad (10)$$

where operator $\text{abs}(\cdot)$ returns a vector that contains the absolute values of the input-vector elements, and operator $\text{diag}(\cdot)$ returns a vector that contains the diagonal elements of the input matrix. If condition (10) is not satisfied, it may be possible to further reduce cost function (5) by using an iterative approach. Specifically, the GCM is relinearized about $\boldsymbol{\eta}^a$ instead of $\mathbf{0}$, matrix \mathbf{G} is recomputed, and a new solution is sought.

3. Ocean state estimation example

The Green's function approach has been applied to the calibration of a general circulation model, which is used for quasi-operational analysis of the time-evolving ocean circulation. This analysis is a product of the consortium for Estimating the Circulation and Climate of the Ocean (ECCO), it is maintained at the Jet Propulsion Laboratory (JPL), it is updated approximately once per week, it is freely available (<http://ecco.jpl.nasa.gov>), and it is being used for a variety of science applications (e.g., Dickey et al. 2002; Fukumori et al. 2004; Gross et al. 2003; Lee and Fukumori 2003; McKinley et al. 2003). The discussion that follows is not meant to be the definitive description of the ECCO/JPL ocean circulation analysis; it is only meant to provide a concrete example for the application of the Green's function approach.

a. Baseline 1991–2000 integration

The ECCO/JPL near-real time analysis is based on a quasi-global configuration of the Massachusetts Institute of Technology General Circulation Model (MIT GCM; Marshall et al. 1997). The model grid has 360 ×

224 horizontal grid cells. Zonal grid spacing is 1° of longitude. Meridional grid spacing is 0.3° of latitude within $\pm 10^\circ$ of the equator and increases to 1° latitude outside the Tropics, as shown on the left panel of Fig. 1. There are 46 vertical levels with thicknesses ranging from 10 to 400 m down to a maximum depth of 5815 m, as shown on the right panel of Fig. 1. Figure 2 shows the model bathymetry. Ocean regions north of 73°N and south of 73°S are not represented in order to permit a 1-h integration time step. The model employs the K-Profile Parameterization (KPP) vertical mixing scheme of Large et al. (1994) and the isopycnal mixing schemes of Redi (1982) and Gent and McWilliams (1990) with surface tapering as per Large et al. (1997). Laplacian diffusion and friction are used except for horizontal friction, which is biharmonic. Lateral boundary conditions are closed. No-slip bottom, free-slip lateral, and free surface boundary conditions are employed. Surface freshwater fluxes are applied as virtual salt fluxes.

The baseline integration spans 1991 to 2000 and is forced at the surface with 12-hourly wind stress and with daily heat and freshwater fluxes from the National Centers for Environmental Prediction (NCEP) meteorological reanalysis (Kistler et al. 2001) with the following modifications:

- 1) The 1980–97 time-mean NCEP fluxes are subtracted and replaced with the 1945–93 time-mean Comprehensive Ocean–Atmosphere Data Set (COADS) fluxes (Woodruff et al. 1998).
- 2) The 1945–93 time-mean COADS heat and freshwater fluxes have further been adjusted so that the spatial integral is zero over the model domain.
- 3) Model sea surface temperature (SST) is relaxed to

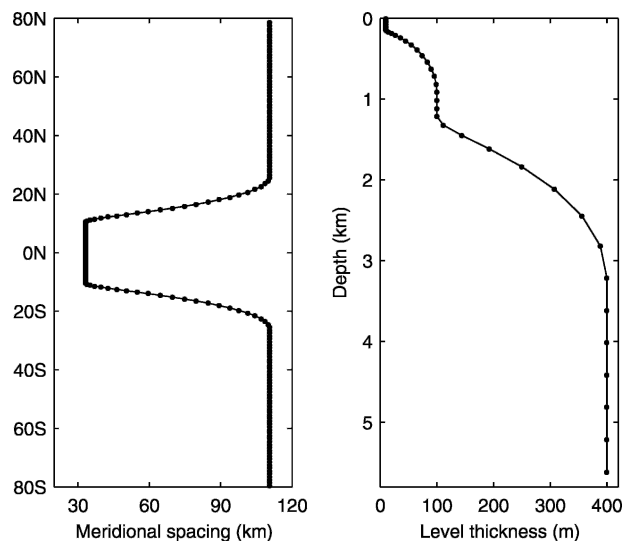


FIG. 1. The ocean GCM has 360 zonal by 224 meridional by 46 vertical grid cells. Zonal grid spacing is 1°. (left) Meridional grid spacing as a function of latitude, and (right) level thickness as a function of depth.

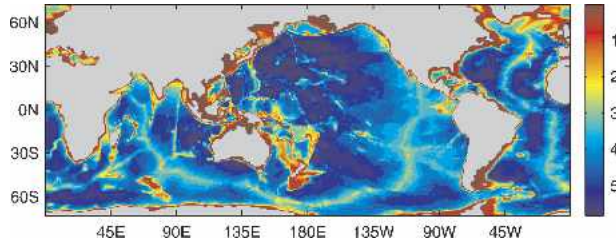


FIG. 2. Model bathymetry in km. The ocean domain spans 73°S to 73°N and excludes the Arctic Ocean.

NCEP SST using the dQ/dT formulation of Barnier et al. (1995), where Q is heat flux and T is SST.

- 4) Shortwave radiation is depth-penetrating using the formula of Paulson and Simpson (1977).
- 5) Any model temperature that becomes less than -1.8°C is reset to -1.8°C in order to simulate the freezing of seawater.
- 6) Sea surface salinity (SSS) is relaxed to monthly mean SSS from the National Oceanographic Data Center (NODC) World Ocean Atlas 1998 (WOA98) with a relaxation constant of 60 days.

Isopycnal diffusivity and isopycnal thickness diffusivity is $500 \text{ m}^2 \text{ s}^{-2}$. Hereinafter, isopycnal diffusivity also refers to isopycnal thickness diffusivity, which is set to the same value. Vertical diffusivity is $5 \times 10^{-6} \text{ m}^2 \text{ s}^{-2}$. Horizontal and vertical viscosity are $10^{13} \text{ m}^4 \text{ s}^{-1}$ and $10^{-4} \text{ m}^2 \text{ s}^{-2}$, respectively. The model is initialized from rest and from the WOA98 temperature and salinity climatology and integrated for 10 yr using the 1980–97 mean NCEP seasonal cycle. It is then integrated from January 1980 to December 1990 using real-time fluxes to obtain January 1991 initial conditions for the baseline integration. These particular choices need not be further justified here, since they are superseded later in this manuscript using the Green's function approach. Suffice to say that they were the result of dozens of trial-and-error experiments, over the course of several years, by a handful of experienced physical oceanographers.

b. Data used to constrain the baseline integration

The data that are used to constrain the baseline integration are observations of sea surface height variability and a collection of vertical temperature profiles. Sea surface height data are from the National Aeronautics and Space Administration Goddard Space Flight Center (NASA GSFC) Pathfinder Topographic Ocean Experiment (TOPEX)/Poseidon Altimetry Version 9.1 (<http://podaac.jpl.nasa.gov>). Specifically, colinear sea surface height data are used, which are georeferenced to a specific ground track and are given at 1-s intervals, approximately every 6 km along each track. The data are corrected for all known geophysical, media, and instrument effects, including tides and atmo-

spheric loading. The Pathfinder data are further bin averaged along each track, consistent with the model resolution.

Vertical temperature profile data from expendable bathythermograph (XBT) and from the Tropical Atmosphere Ocean (TAO) array are processed, quality checked, and made available by D. Behringer (2002, personal communication). These data are complemented with temperature profiles from the World Ocean Circulation Experiment (WOCE), from the Hawaii Ocean Time Series (HOTS), from the Bermuda Atlantic Time Series (BATS), and from Profiling Autonomous Lagrangian Circulation Explorer (PALACE) floats. Figures 3 and 4 show, respectively, the horizontal and vertical data distributions. For this study, the temperature data are bin averaged inside each model grid box and for 10-day intervals spanning 1 January 1992 to 31 December 2000. In all there are 498 277 vertical temperature profiles, which are bin averaged into 5 227 445 space–time bins.

c. Sequential smoother and adjoint method

The baseline integration described in section 3a was initially constrained with the data of section 3b using the partitioned sequential smoother of Fukumori (2002). As currently implemented, the Fukumori (2002) smoother is used to estimate adiabatic corrections due to errors in the time-varying surface wind stress. But the smoother has not yet been extended to handle model biases or to correct errors in surface heat and freshwater fluxes and in diabatic processes.

A powerful methodology for removing model biases and for correcting errors in surface heat and freshwater fluxes and in diabatic processes is provided by the adjoint model (e.g., Stammer et al. 2003). But at the time that this work was carried out, the available computer resources were insufficient for a complete 1991–2000 adjoint-model optimization using the model configuration just described. Based on the experience of Stammer et al. (2003), a complete adjoint-method optimization may have required the equivalent of some 500 forward-model integrations over the 1991–2000 estimation

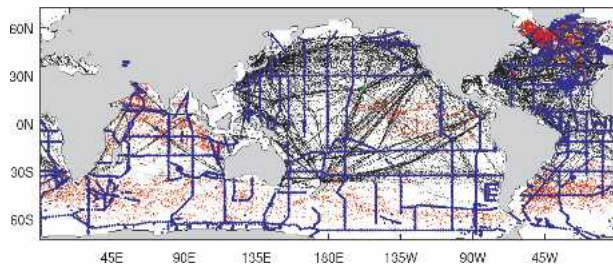


FIG. 3. Horizontal distribution of temperature profiles. Black dots indicate locations of XBT and TAO profiles; blue dots indicate locations of WOCE profiles; red dots indicate locations of PALACE profiles; and green and magenta dots indicate locations of HOTS and BATS profiles, respectively.

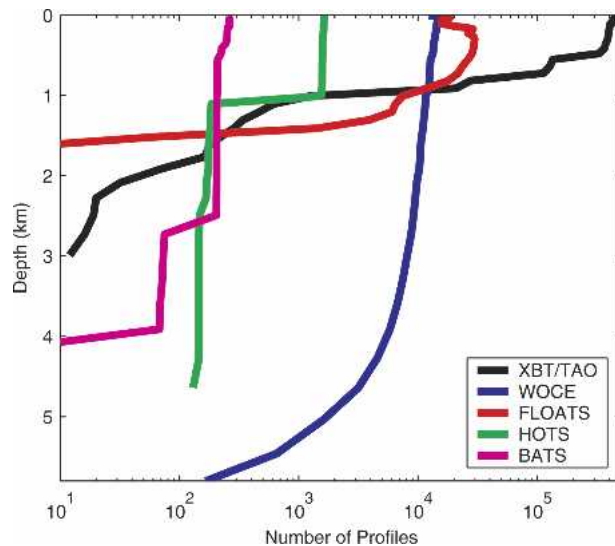


FIG. 4. Vertical distribution of available temperature data.

period, that is, approximately 100 forward- and adjoint-model integrations, with each adjoint-model integration requiring approximately 4 times as much time to complete as a forward-model integration. Also the computer memory and disk storage requirements for an adjoint-model optimization are larger, typically by a factor of 10, or more, than those of the forward integration. This is because of the need to store intermediary model variables in order to reduce recomputations (Heimbach et al. 2002).

It should also be pointed out that the particular GCM configuration, which is used to carry out the work described here, does not have a well-defined tangent linear for periods longer than about 10 days. This is because of sensitivity issues related to the vertical and isopycnal mixing parameterizations. Therefore it is not possible to directly apply the adjoint-model method: some modifications or simplifications of the GCM code are required. The Green's function approach is more robust, as is demonstrated below, because it relies on an approximate linearization of the GCM, not on the exact tangent-linear model.

Finally, the development of a partitioned smoother

or of an adjoint-method optimization requires substantial manpower and expertise. By comparison, the computation of model Green's functions is straightforward. A model Green's function is derived by perturbing a model parameter relative to the baseline integration and then integrating the model forward from 1991 to 2000. That is, the computation of a model Green's function is equivalent to the computation of a model sensitivity experiment.

All the above reasons motivated the development of the Green's function approach, which is described next, as a way to remove model biases and to correct errors in surface heat and freshwater fluxes and in diabatic processes for the ECCO/JPL ocean circulation analysis.

4. A first Green's function optimization

A first test of the Green's function approach is carried out using six sensitivity experiments. For experiments 1–3 the baseline 1991–2000 integration of section 3a is repeated with perturbed vertical diffusivity, vertical viscosity, and isopycnal diffusivity coefficients, as indicated in Table 1. For experiment 4, the time-mean wind stress of the baseline integration is replaced by a time-mean wind stress derived from NASA quick scatterometer (QuikSCAT) data (W. Tang 2002, personal communication). For experiment 5, a temperature perturbation is generated by optimal interpolation (OI) of the observed model-data difference and added to the 1991 initial conditions. For experiments 6, the model is reinitialized in 1991 from the January WOA98 temperature and salinity climatology. In terms of the notation of section 2, $G(\mathbf{0})$ in (7) corresponds to the baseline 1991–2000 integration sampled at the locations and times of the temperature data; $G(\mathbf{e}_j)$ in (7) represents the six sensitivity experiments of Table 1, also sampled at the locations and times of the temperature data. The data kernel matrix, \mathbf{G} in (6), (8), and (9), is a tall, skinny matrix, with six columns and a number of rows equal to the number of data, 10^4 randomly selected observations out of the total of 5×10^6 bin-averaged temperature observations.

a. Cost function

An important step for optimization studies is the definition of cost function J in (5) and, in particular, the

TABLE 1. List of sensitivity experiments for the first Green's function optimization. Column 3 lists the baseline parameters. Column 4 lists the perturbed parameters for each of six sensitivity experiments. Columns 5–7 list the optimized parameters and uncertainty for three different cost functions. For experiments 4–6, the optimized parameters are indicated in terms of fractional perturbation QSCAT-COADS, SPINUP-OI, and SPINUP-WOA98, respectively.

Expt	Parameter	Baseline	Perturbation	Case 1	Case 2	Case 3
1	Vertical diffusivity ($10^{-6} \text{ m}^2 \text{ s}^{-2}$)	5	10	15.1 ± 2	15.2 ± 0.8	15.4 ± 0.8
2	Vertical viscosity ($10^{-6} \text{ m}^2 \text{ s}^{-2}$)	100	200	68 ± 60	59 ± 22	46 ± 28
3	Isopycnal diffusivity ($\text{m}^2 \text{ s}^{-2}$)	500	400	605 ± 48	592 ± 18	572 ± 26
4	Time-mean wind stress	COADS	QSCAT	0.22 ± 0.18	0.21 ± 0.06	0.43 ± 0.08
5	Initial temperature	SPINUP	OI	0.10 ± 0.14	0.17 ± 0.06	0.11 ± 0.08
6	Initial temperature and salt	SPINUP	WOA98	0.75 ± 0.14	0.67 ± 0.06	0.71 ± 0.08

specification of prior error covariance matrices \mathbf{Q} and \mathbf{R} (e.g., Menemenlis and Chechelnitsky 2000). For the Green's function approach, the number of observations is generally much larger than the number of parameters being estimated, which simplifies this task. First, the small number of control parameters limits the solution's degrees of freedom; therefore the choice of \mathbf{Q} and of \mathbf{R} , if they are reasonable, is not expected to change the solution much. Second, the data kernel matrix \mathbf{G} is small enough to be defined explicitly; therefore many interesting properties of the solution—for example, the model resolution matrix—can be derived and evaluated. Third, the solution of (8) and (9), once the kernel matrix \mathbf{G} has been derived, is trivial; therefore it is possible to test the impact of particular choices of \mathbf{Q} and of \mathbf{R} , as is done next.

For the first Green's function optimization we test three different cost functions. In all three cases the form of the cost functions is

$$J = \sum_i \left(\frac{y_i^o - x_i}{\sigma_i} \right)^2, \quad (11)$$

where y_i^o represents temperature data, x_i is the model estimate, σ_i^2 is the assumed data error variance, and subscript i represents a specific location and time. Cost function (11) implies that the data-error covariance matrix \mathbf{R} is diagonal and that there is no a priori information about the parameters to be optimized, that is, $\mathbf{Q}^{-1} = \mathbf{0}$. The assumption of diagonal \mathbf{R} is justified because the temperature data, which are already bin averaged inside each model grid box and for 10-day intervals, are further decimated so that each optimization is carried out using 10^4 randomly selected observations out of the total of 5×10^6 bin-averaged temperature observations. The agnostic assumption that $\mathbf{Q}^{-1} = \mathbf{0}$ has little impact on the solution because the minimization problem is highly overdetermined.

The three cost functions that are tested are labeled cases 1–3. For case 1, the a priori error variance, σ_i^2 in (11), is assumed horizontally homogeneous and equal to the data variance at each depth, as shown in Fig. 5. This assumption is a conservative upper bound for data and model representation errors. For case 2 the a priori error variance is assumed horizontally homogeneous but equal to the variance of the model-data difference at each depth, also shown in Fig. 5. Finally, for case 3 the mean a priori error variance at each depth is also proportional to the variance of the model-data difference, as is that of case 2, but it is scaled horizontally by the sea level anomaly variance observed by TOPEX/Poseidon (Fig. 6). For case 3, the global-mean a priori error variance is further scaled using the following ad hoc approach. Two hundred different estimates are obtained using two hundred randomly sampled subsets of the data. The global-mean a priori error variance is then adjusted so that the a posteriori uncertainty vari-

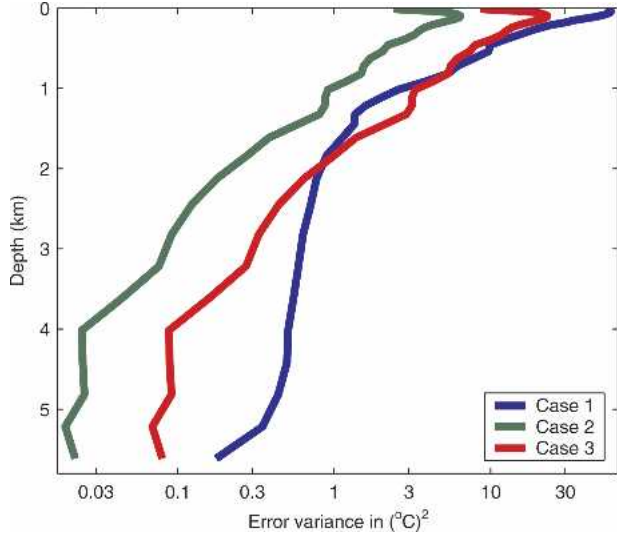


FIG. 5. Assumed vertical profiles of a priori error variance. Case 1 is the mean data variance at each depth. Case 2 is the mean variance of the model-data difference at each depth. Case 3 is proportional to the variance of the model-data difference but has further been scaled as described in the text.

ance of the estimates—that is, the diagonal elements of matrix \mathbf{P} in (9)—are approximately equal to the diagonal elements of $\text{cov}(\boldsymbol{\eta}^a)$, the sample covariance of the two hundred estimates.

Columns 5–7 in Table 1 list the optimized parameters and the uncertainties for the three different a priori assumptions described above. Uncertainty here refers to twice the square root of the diagonal elements of matrix \mathbf{P} in (9), the 95% confidence level if the errors are normally distributed. Admittedly, all three a priori error variance estimates are ad hoc. What matters for the present discussion is that the three cases are different, ranging from likely upper bound (case 1), lower bound (case 2), and something in between (case 3). Yet all three cases give similar estimates; the error bars overlap at the 95% confidence level. In particular, the optimized estimates of vertical viscosity and diffusivity and also of initial temperature and salinity conditions

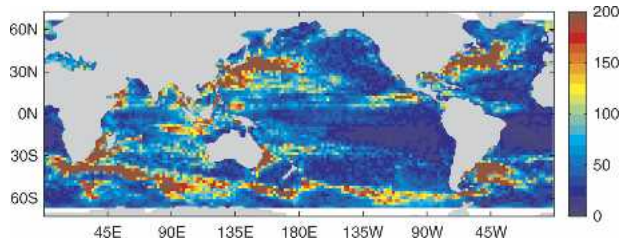


FIG. 6. Variance of sea level anomaly in cm^2 observed by the TOPEX/Poseidon altimeter during the 1993–2000 period. This map provides horizontal scaling for the case-3 a priori error variance, which is used for weighting the data errors in the cost function.

are radically different from those that are used in the baseline integration.

Because of coarse resolution, artificial northern boundary conditions, and lack of an interactive sea ice model, the present model configuration is not expected to be very realistic at high latitudes. Therefore, for the remainder of this article, we use the spatially varying definition for the a priori error variance—that of case 3, which downweights the high latitudes.

b. Linear approximation

The fundamental assumption that underlies the Green's function approach is that the estimation problem can be linearized relative to the baseline integration. That is, the optimal solution can be obtained as a linear combination of the baseline and sensitivity experiments. The extent to which this assumption is valid can be evaluated by comparing the optimal linear combination of the baseline and sensitivity experiments with a new model integration, which is carried out using the optimized parameters.

Assuming linearity, the expected cost function reduction relative to the baseline integration is 30% for the case-3 parameters, those of column 7 in Table 1. The actual cost function reduction, when the case-3 parameters are used to carry out a new model integration, is 33%. This is 3% better than what would be expected for a perfectly linear problem. While in general we do not expect such substantial cost function reduction, this preliminary optimization demonstrates that exact linearity is not required for the Green's function approach to work and that the optimization of a small number of carefully chosen parameters can have a large positive impact on the solution.

On average, for the first Green's function optimization, the errors due to nonlinearity are approximately 25% of the assumed a priori errors in the data and in the model; that is, the right-hand side of (10) is approximately 4 times larger than the left-hand side. Therefore the linear approximation is satisfied and no further iterations are needed in order to optimize the six parameters listed in Table 1.

c. Linear dependence

Once the linear approximation has been validated, the kernel matrix \mathbf{G} , which is explicitly computed in the

Green's function approach, can be used to ask many interesting and important "what if" questions. This capability is a key advantage of the Green's function approach. Below we use \mathbf{G} to determine the consequences of estimating the parameters of Table 1 one at a time, to determine the relative contribution of each parameter to cost function reduction, and to infer the robustness of the estimates that have been obtained.

Table 2 lists estimates from one-at-a-time optimizations and compares the results to those of case 3. The table shows that the one-at-a-time estimates differ substantially from those of case 3. This is because the parameter estimates are linearly dependent on each other. Therefore the parameters cannot be estimated independently. Note that the largest impact on cost function reduction comes first from the vertical diffusivity parameter and second from the initial conditions. This will be explained in sections 5f and 5g as resulting primarily from reduction of drift in the upper pycnocline and from compensation of model bias accumulated in that same region during model spinup.

To gauge the relative contribution of each parameter to cost function reduction, additional optimizations are carried out using only five out of the six possible parameters. The results of these optimizations are summarized in Table 3. The table shows that by optimizing only five of the six parameters, the cost function reduction ranges from 19.8% to 29.7% as compared to 29.8% for case 3, in which all six parameters are optimized. In order of decreasing importance for cost function reduction, the parameters are 1) vertical diffusivity, 2) initial conditions, 3) time-mean wind stress, 4) isopycnal diffusivity, and 5) vertical viscosity.

The optimizations summarized in Tables 2 and 3 can also be used to gauge the likely impact of increasing the number of control parameters, that is, the number of degrees of freedom of the optimization. For example, one may infer that the estimate of vertical diffusivity is relatively robust since its range is limited: 15.0×10^{-6} to $17.4 \times 10^{-6} \text{ m}^2 \text{ s}^{-2}$. By comparison the estimate of vertical viscosity is not very robust since it ranges from 6.0×10^{-6} to $348 \times 10^{-6} \text{ m}^2 \text{ s}^{-2}$.

5. A second Green's function optimization

The encouraging results from the six-parameter optimization discussed above motivated the computation

TABLE 2. Optimized parameters for case 3 (Table 1) are compared to parameters estimated one at a time. The last row displays the cost function reduction in percent assuming that the problem is linear. Because the parameter estimates are linearly dependent, the one-at-a-time estimates differ substantially from those of case 3.

Parameter	Case 3	Case 4	Case 5	Case 6	Case 7	Case 8	Case 9
Vertical diffusivity ($10^{-6} \text{ m}^2 \text{ s}^{-2}$)	15.4	17.4	—	—	—	—	—
Vertical viscosity ($10^{-6} \text{ m}^2 \text{ s}^{-2}$)	46	—	348	—	—	—	—
Isopycnal diffusivity ($\text{m}^2 \text{ s}^{-2}$)	572	—	—	399	—	—	—
Time-mean wind stress	0.43	—	—	—	0.72	—	—
Initial temperature	0.11	—	—	—	—	0.60	—
Initial temperature and salt	0.71	—	—	—	—	—	2.5
Cost function reduction (%)	29.8	19.4	0.58	0.14	5.42	6.46	14.2

TABLE 3. Optimized parameters for case 3 (Table 1) are compared to estimates for optimizations where one of the six parameters is not used. The last row displays the cost function reduction in percent assuming that the problem is linear.

Parameter	Case 3	Case 10	Case 11	Case 12	Case 13	Case 14	Case 15
Vertical diffusivity ($10^{-6} \text{ m}^2 \text{ s}^{-2}$)	15.4	—	15.0	15.2	16.4	15.5	16.9
Vertical viscosity ($10^{-6} \text{ m}^2 \text{ s}^{-2}$)	46	115	—	6	54	47	41
Isopycnal diffusivity ($\text{m}^2 \text{ s}^{-2}$)	572	540	599	—	579	569	571
Time-mean wind stress	0.43	0.64	0.42	0.44	—	0.43	0.38
Initial temperature	0.11	0.23	0.10	0.08	0.13	—	0.42
Initial temperature and salt	0.72	0.90	0.72	0.71	0.69	0.76	—
Cost function reduction (%)	29.8	19.8	29.5	29.3	27.9	29.7	24.5

of 20 additional model sensitivity experiments. These additional experiments are summarized in Table 4. Note that these 20 new sensitivity experiments were computed relative to the case-3 solution of the first Green's function optimization and that they include a repeat of all six sensitivity experiments listed in Table 1. The end result of this second optimization is a further 10% cost function reduction, as indicated in Table 5. The resulting estimates of vertical mixing coefficients, surface heat and freshwater fluxes, isopycnal diffusivity, surface wind stress, and initial conditions are discussed below, followed by an analysis of improvements in bias, drift, and explained variance relative to earlier solutions and to data.

a. Vertical mixing

Sensitivity experiments 1–4 in Table 4 pertain to the representation of vertical mixing in the model. Notice that the background vertical diffusivity, which had been deemed a relatively robust estimate in the earlier discussion, remains unchanged with a value of $(15.1 \pm 0.1) \times 10^{-6} \text{ m}^2 \text{ s}^{-2}$. This value is consistent with inferences from microstructure and tracer studies (e.g., Kelley and Van Scoy 1999, and references therein).

The estimate of background vertical viscosity is $(18 \pm 3) \times 10^{-6} \text{ m}^2 \text{ s}^{-2}$, which is approximately 6 times smaller than the value of $10^{-4} \text{ m}^2 \text{ s}^{-2}$, which is often used for ocean modeling (e.g., Large et al. 2001). A possible explanation for this difference is that the optimal background vertical viscosity is strongly dependent on the values of other model variables, in particular on the values of vertical and isopycnal diffusivity.

Two additional parameters of the Large et al. (1994) KPP scheme, Ri_c and Ri_0 , have been estimated; Ri_c is the critical bulk Richardson number, which sets the depth of the oceanic boundary layer. The estimate of 0.354 ± 0.004 is 18% larger than the value suggested by Large et al. (1994). This compensates, in part, for shallow boundary layers depths in the baseline integration relative to the data; Ri_0 is a threshold gradient Richardson number for shear instability vertical mixing, which is especially important for equatorial dynamics. The estimated value of 0.699 ± 0.008 is the same as that suggested by Large et al. (1994).

b. Surface heat and freshwater fluxes

Experiments 5 and 6 are used to adjust the surface salinity and temperature relaxation terms. The estimates shown in Table 4 indicate that the baseline values of the relaxation coefficients are too weak for salinity and too strong for temperature. Figure 7 compares the mean and standard deviation of the resulting estimates of surface heat and freshwater fluxes with those from the NCEP reanalysis. The corrections to the time-mean surface fluxes are substantial, up to 100 W m^{-2} for heat and 2 m yr^{-1} for freshwater, which are values comparable to the time-mean fields themselves.

It is interesting to compare the estimated time-mean surface flux corrections (Figs. 7b and 7f) to the estimates obtained independently by Stammer et al. (2004, their Fig. 3) using the adjoint method. Except for the equatorial Pacific, the similarities of the two estimates both in pattern and in magnitude are striking. The principal differences between the two estimates occur near

TABLE 4. List of sensitivity experiments and optimized parameters for the second Green's function optimization. For experiment 6, the optimized parameter is indicated as a factor multiplying the $\partial Q/\partial T$ fields of Barnier et al. (1995).

Expt	Parameter	Baseline	Optimized
1	Vertical diffusivity ($10^{-6} \text{ m}^2 \text{ s}^{-2}$)	5	15.1 ± 12
2	Vertical viscosity ($10^{-6} \text{ m}^2 \text{ s}^{-2}$)	100	17.7 ± 3.0
3	Ri_c , boundary layer depth	0.300	0.354 ± 0.004
4	Ri_0 , shear instability	0.700	0.699 ± 0.008
5	Salinity relaxation (days)	60	44.5 ± 1.2
6	Temperature relaxation ($\partial Q/\partial T$)	1.000	$1.630 \pm .008$
7–10	Isopycnal diffusivity ($\text{m}^2 \text{ s}^{-2}$)	500	Linear combination
11–14	Surface wind stress	NCEP/COADS	Linear combination
15–20	Initial conditions	SPINUP	Linear combination

TABLE 5. Cost function reduction relative to baseline integration.

Integration	Cost function	Reduction (%)
Baseline	5606	—
Optimization 1	3773	32.7
Optimization 2	3191	43.1

the equator where the meridional grid spacing of the present study is higher than that of Stammer et al. (2004), that is, 35 km instead of 110 km. A detailed comparison of the two solutions is in preparation. Both the present results and those of Stammer et al. (2004) suggest that NCEP reanalysis heat and freshwater fluxes are suboptimal surface boundary conditions for ocean modeling.

c. Isopycnal diffusivity

Isopycnal diffusivity is estimated as the linear combination of four sensitivity experiments. The objective is to obtain a crude estimate of the time-independent horizontal and vertical variations of this parameter. The first sensitivity experiment is a constant perturbation, similar to experiment 3 in the first Green's function optimization. The second experiment is a vertically homogeneous but spatially varying perturbation. Following the suggestion of Holloway (1986) the spatial variation of this perturbation is proportional to $gh/|f|$, where g is the acceleration of gravity, h is the standard deviation of observed sea surface height variations after removing tidal effects and the seasonal cycle, and $f = 2\Omega \sin\phi$ is the Coriolis parameter, where Ω is the

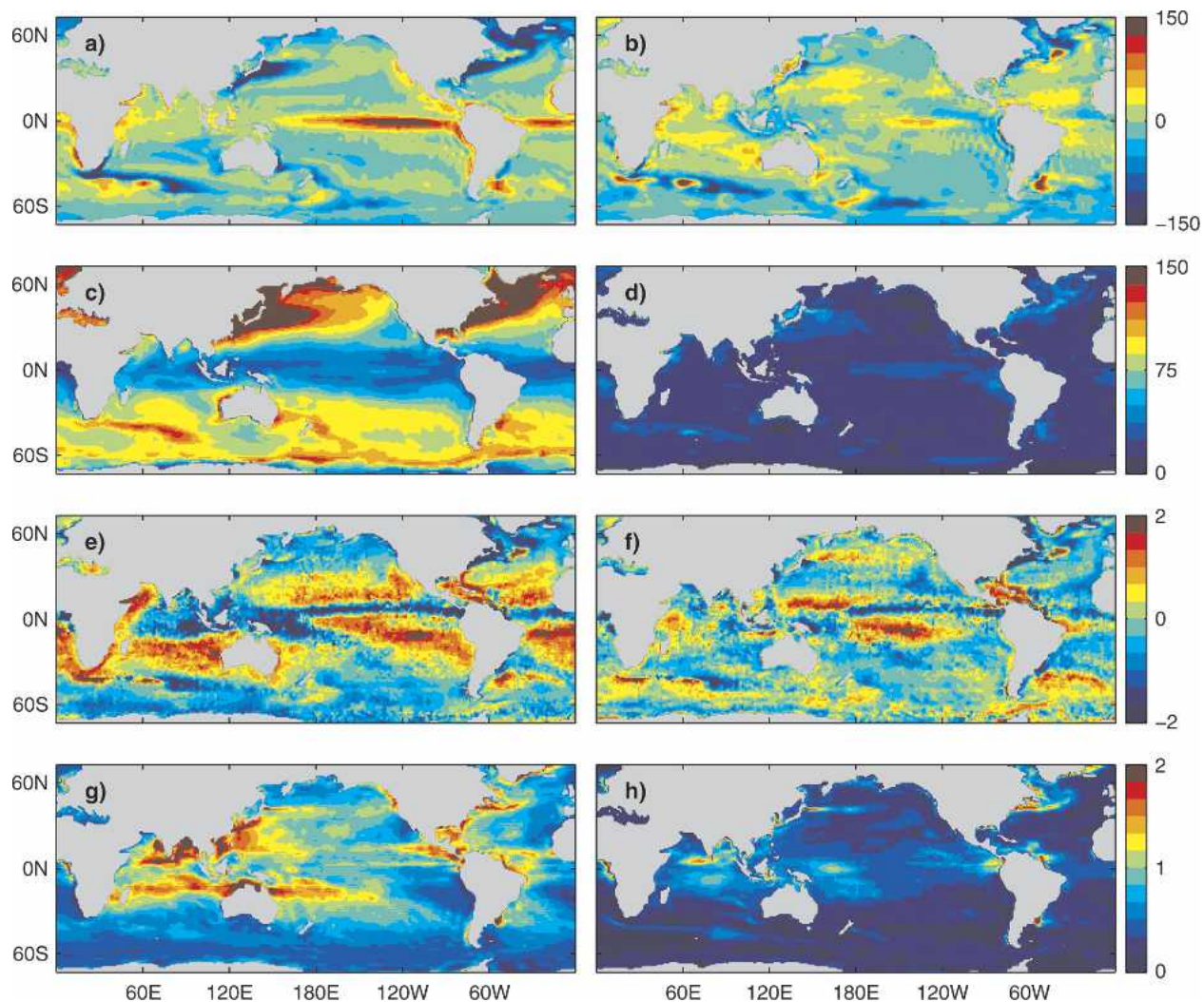


FIG. 7. Comparison of estimated surface heat and freshwater fluxes with NCEP reanalysis for the 1993–2000 period: (a) estimate of mean heat flux entering the ocean; (b) (a) minus NCEP; (c) standard deviation of estimated surface heat flux; (d) standard deviation of difference with NCEP; (e) estimate of mean evaporation minus precipitation minus runoff; (f) (e) minus evaporation plus precipitation from NCEP; (g) standard deviation of the estimated evaporation minus precipitation minus runoff; (h) standard deviation of the difference with NCEP. Units are W m^{-2} for heat and m yr^{-1} for freshwater.

earth's rotation rate and ϕ is latitude; in the Tropics, 23°S to 23°N , $|f|$ is set equal to $5.7 \times 10^{-5} \text{ s}^{-1}$ for this computation. The third and fourth sensitivity experiments are also spatially varying as per Holloway (1986) but with exponentially decaying amplitude in the vertical, $\exp(-z/500)$ and $\exp(-z/1000)$, respectively, where z is the depth in meters.

Figures 8 and 9 display, respectively, a horizontal map of estimated isopycnal diffusivity at 1000-m depth and vertical profiles of minimum and maximum diffusivity. The estimates range from 550 to $1350 \text{ m}^2 \text{ s}^{-2}$ and straddle the value of $800 \text{ m}^2 \text{ s}^{-2}$ suggested by Large et al. (1997) but are considerably lower than the 1500 to $4000 \text{ m}^2 \text{ s}^{-2}$ range that had been inferred by Holloway (1986) using satellite altimeter data. In the vertical, the estimates exhibit a 5%–35% decrease near the surface. This is contrary to the a priori expectation that the estimated isopycnal diffusivity coefficient would be larger near the surface where the eddy kinetic energy is higher. The estimated decrease in near-surface isopycnal diffusivity is in addition to the Large et al. (1997) surface-tapering scheme, which has also been applied in this study.

d. Surface wind stress

Surface wind stress is estimated as a linear combination of four sensitivity experiments. The first two experiments perturb the time-mean wind stress while preserving the variability of the NCEP reanalysis. The next two experiments perturb the time-variable wind stress. Note that in the baseline integration, the time-mean NCEP wind stress has already been replaced with a time-mean wind stress derived from the COADS climatology, as discussed in section 3a.

Specifically, the first sensitivity experiment, labeled QSCAT, replaces the time-mean wind stress of the baseline integration with a time-mean wind stress derived from QuikSCAT data (W. Tang 2002, personal communication). The second sensitivity experiment, labeled ERSMEAN, replaces the time-mean wind stress with a wind product derived from European Remote Sensing (ERS) satellites and obtained from the ERS Processing and Archiving Facility (CERSAT) at the French Research Institute for Exploration of the Sea (IFREMER). The third sensitivity experiment, labeled

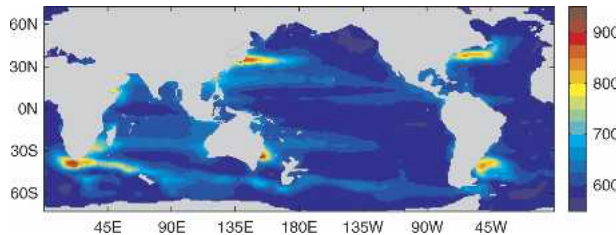


FIG. 8. Estimated isopycnal diffusivity in $\text{m}^2 \text{ s}^{-1}$ at the 1000-m depth.

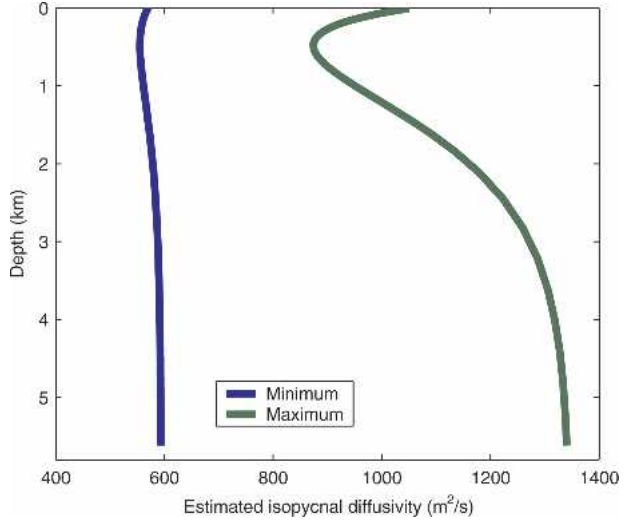


FIG. 9. Vertical profile of estimated isopycnal diffusivity.

ERS, includes both the time mean and the time variability of the CERSAT wind product. Finally, the fourth sensitivity experiment, labeled SM, replaces the time-variable winds with those estimated by the approximate smoother described in section 3c.

The optimal surface wind stress estimate is

$$\tau(\mathbf{r}, t) = \bar{\tau}(\mathbf{r}) + \tau'(\mathbf{r}, t), \quad (12)$$

where

$$\begin{aligned} \bar{\tau}(\mathbf{r}) = & 0.55 \text{ COADS} + 0.56 \text{ ERSMEAN} \\ & - 0.11 \text{ QSCAT} \end{aligned} \quad (13)$$

is the time-mean wind stress,

$$\tau'(\mathbf{r}, t) = 1.02 \text{ SM} + 0.41 \text{ ERS} - 0.43 \text{ NCEP} \quad (14)$$

is the time-variable wind stress, and \mathbf{r} and t are space and time coordinates, respectively. The wind stress estimates are compared to the NCEP reanalysis in Fig. 10. The wind stress estimates can also be compared to those obtained independently by Stammer et al. (2004; Fig. 9) using the adjoint method. In the large scale, both estimates show an increase in the trade winds over the tropical Pacific and a weakening of the midlatitude winds, especially above the Southern Ocean. In terms of meridional wind stress changes, both estimates indicate a smaller poleward component at latitudes higher than 30°N . The principal differences between the two estimates is that the adjoint-model solution contains many small-scale wind stress corrections—especially in western boundary current regions and above the Antarctic Circumpolar Current—that are not present in the Green's function solution.

The estimated time variability of the surface wind stress is very similar to that estimated by the smoother, SM in (14). This is an indication of the consistency and

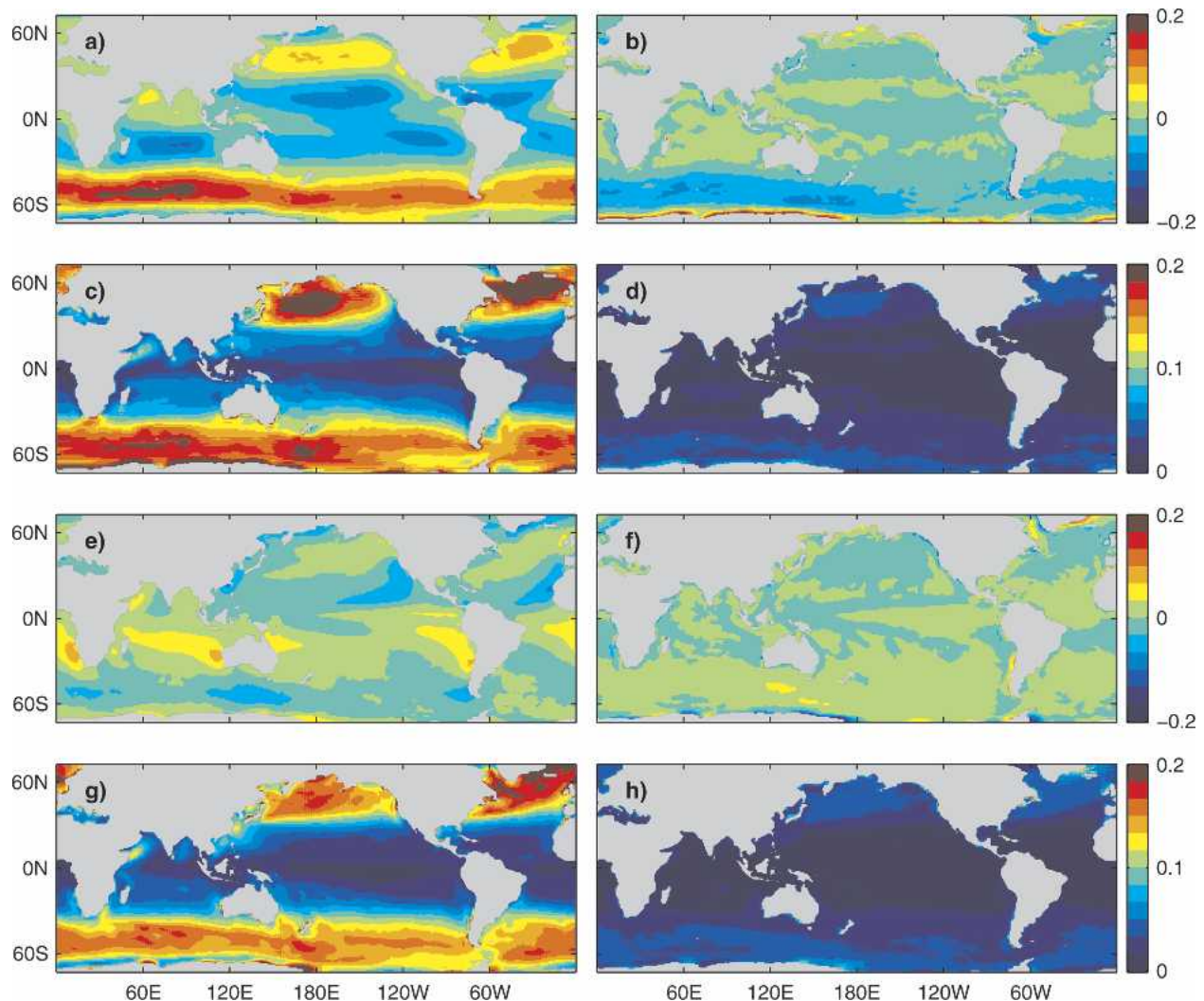


FIG. 10. Comparison of estimated surface wind stress with NCEP reanalysis for the 1993–2000 period: (a) estimate of mean zonal wind stress; (b) (a) minus NCEP; (c) standard deviation of the estimated zonal wind stress; (d) standard deviation of the difference with NCEP; (e) estimate of mean meridional wind stress; (f) (e) minus NCEP; (g) standard deviation of the estimated meridional wind stress; (h) standard deviation of the difference with NCEP. Units are N m^{-2} . Positive values are eastward for zonal wind stress and northward for meridional wind stress.

quality of that estimate. But there nevertheless are some small corrections to the SM wind stress variability that improve the explained sea level variance of the Green's function solution relative to the smoother solution, as will be shown in section 3h.

e. Initial conditions

Initial conditions are estimated as a linear combination of the 20-yr spinup integration, labeled SPINUP and described in section 3a, and of six sensitivity experiments. The objective is to remove model bias while minimizing model drift relative to the data. The first two experiments are a repeat of the OI and climatological (WOA98) initial condition experiments discussed in section 4, but using the diffusivity, viscosity,

and time-mean wind stress estimated by the first Green's function optimization, case 3 in Table 1. A third experiment, labeled WOCE, is initialized from a temperature and salinity climatology derived from WOCE data (Gouretski and Koltermann 2004).

The most substantial drift during spinup, when the model is initialized from a climatology, occurs at high latitudes. In an attempt to minimize this drift, while preserving realistic initial conditions in the Tropics, a fourth sensitivity experiment, labeled BLEND, is initialized from a blend of WOA98 and SPINUP. Between 20°S and 20°N , temperature and salinity is set to WOA98 January values. Poleward of 30°S and 30°N , SPINUP initial conditions are used. There is a gradual, sinusoidal transition between WOA98 and SPINUP in the latitude bands of 20° – 30°N and 20° – 30°S .

The fifth sensitivity experiment, labeled SPINUP2, is initialized from the final conditions of the fourth sensitivity experiment and the sixth sensitivity experiment, labeled SPINUP3, is initialized from the final conditions of the fifth sensitivity experiment. This procedure provides some additional degrees of freedom from which the Green's function minimization can choose suitable initial conditions.

The optimal initial conditions are

$$\begin{aligned} \text{IC} = & 0.53 \text{ WOCE} + 0.30 \text{ WOA98} + 0.18 \text{ SPINUP2} \\ & + 0.07 \text{ SPINUP} + 0.05 \text{ OI} - 0.05 \text{ SPINUP3} \\ & - 0.08 \text{ BLEND}. \end{aligned} \quad (15)$$

The estimated initial temperature and salinity conditions at the 156- and 626-m depths are shown in Fig. 11 and are compared to the WOA98 January climatology.

Except in some isolated regions, for example, the northern edge of the Antarctic Circumpolar Current, the estimated January 1991 temperature is generally warmer than WOA98 in the upper ocean. This warming relative to WOA98 is most pronounced in the central equatorial Pacific, almost 2°C warmer than WOA98, and also in the Gulf Stream and Kuroshio regions.

The estimates of initial salinity also show some large differences, up to 0.2 psu, relative to the January WOA98 climatology. Particularly striking is the plume of increased salinity at 600-m depth in the Atlantic, flowing out of Gibraltar Strait.

f. Bias

Overall, the Green's function optimization substantially improves the time mean, the trend, and the variability of the solution relative to earlier estimates and

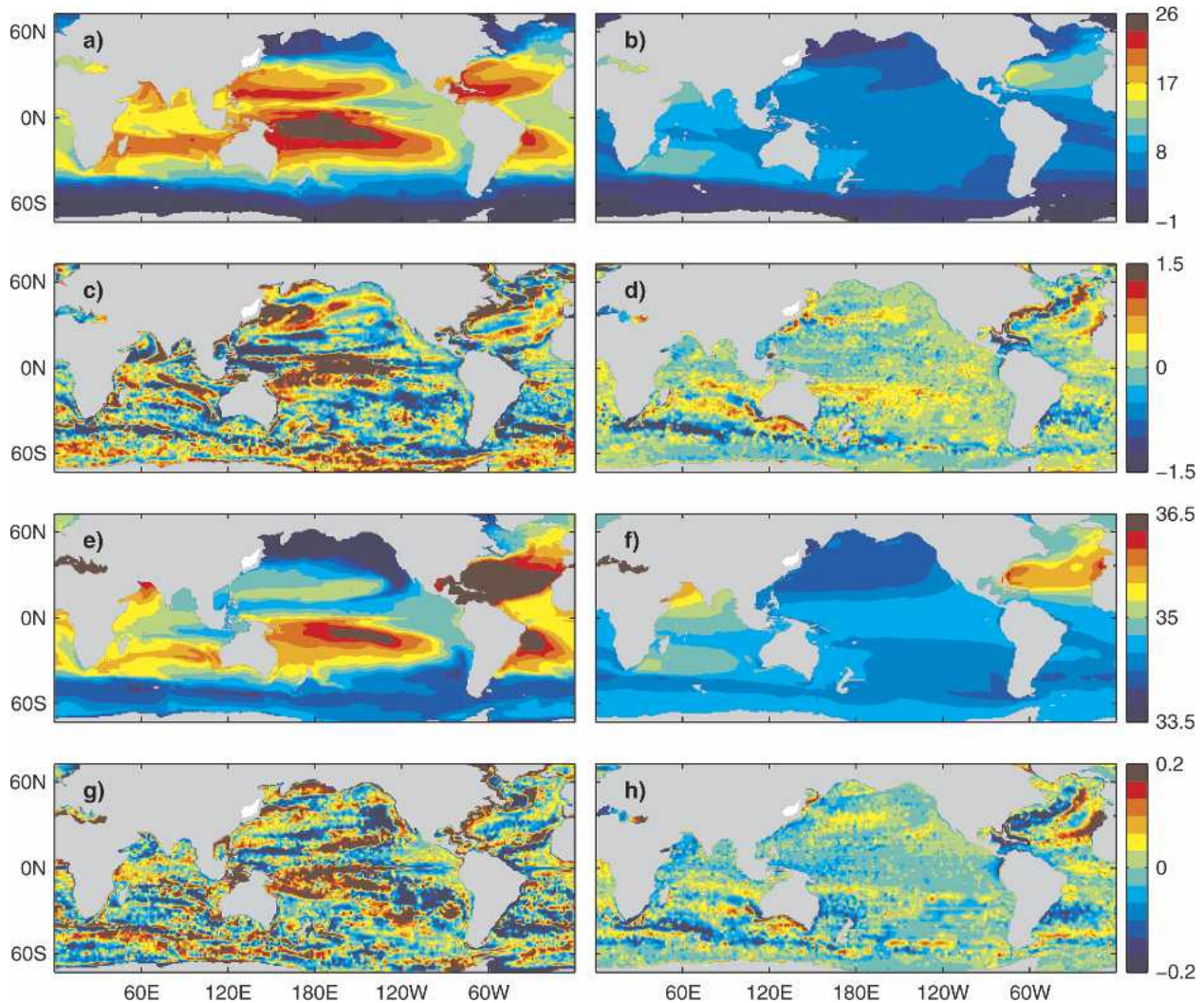


FIG. 11. Comparison of estimated 1991 initial conditions with WOA98 Jan climatology: (a) estimate of temperature at 156 m; (b) estimate of temperature at 626 m; (c) (a) minus WOA98; (d) (b) minus WOA98; (e) estimate of salinity at 156 m; (f) estimate of salinity at 626 m; (g) (e) minus WOA98; (h) (f) minus WOA98. Units are °C for potential temperature and psu for salinity.

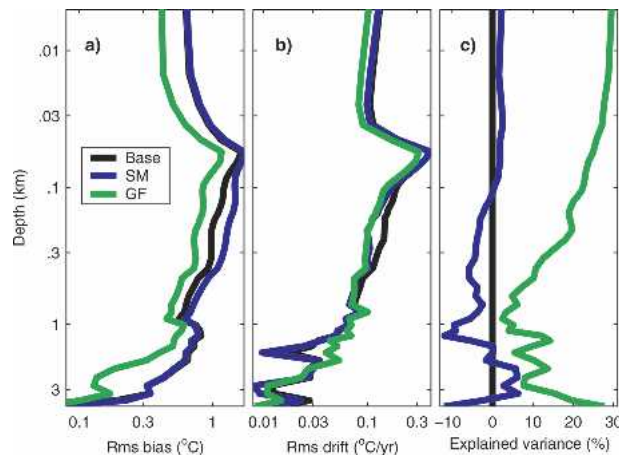


FIG. 12. Comparison of baseline integration (Base), smoother solution (SM), and Green's function solution (GF) to observed temperature profiles: (a) global root-mean-square (rms) difference relative to data; (b) global rms drift relative to data; and (c) percent explained variance of the baseline–data difference.

to data (see Figs. 12–15). The following methodology is used to analyze the temperature data, which are sparse and irregularly sampled in space and in time. The model estimates are first sampled at the exact locations

and times of the temperature data. The temperature data and the model estimates are then binned and analyzed in 20° zonal by 10° meridional grid cells. Global averages are weighted by area and are obtained by averaging the results of all grid cells that contain more than 100 temperature samples.

Figure 12a shows that the Green's function optimization has reduced the bias of the previous solutions relative to data throughout the entire water column. Notice that although the smoother solution corrects the temporal variability, it nevertheless has a measurable impact on the time-mean temperature profile.

The bias reduction of the Green's function solution is most significant at the base of the equatorial thermocline as can be seen by comparing Figs. 13c and 13e. To a large extent this is the result of vertical diffusivity being too weak in the baseline and in the smoother integrations, hence resulting in a thermocline that is too sharp and too shallow relative to data.

Although the bias of the Green's function solution relative to data is decreased on a global average when compared to earlier solutions, there are some regions where the bias remains significant. One of these regions is the Indian Ocean, which is too warm by about 1°C in the Green's function solution at 200-m depth. These residual discrepancies contain information about re-

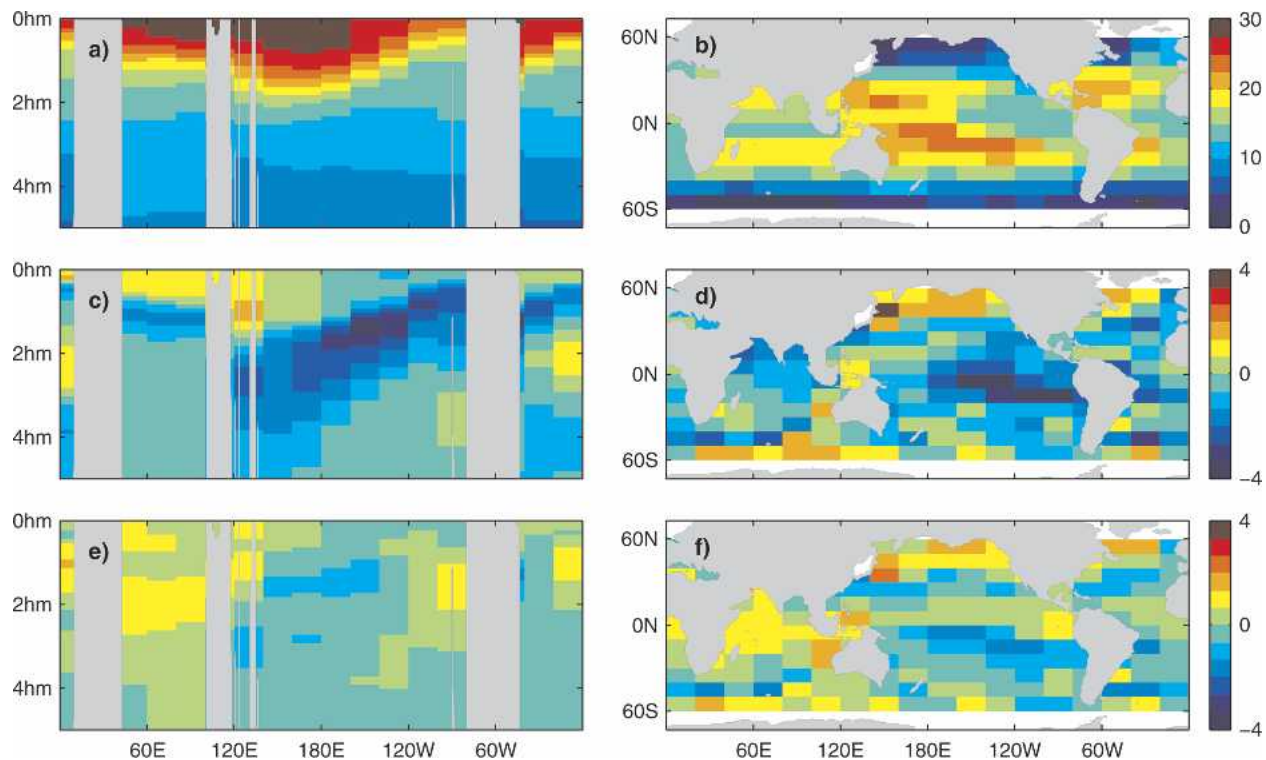


FIG. 13. Time-mean potential temperature, 1993–2000: (a) Green's function estimate at the equator down to 500-m depth; (b) Green's function estimate at the 156-m depth; (c) smoother bias relative to data at the equator; (d) smoother bias relative to data at the 156-m depth; (e) Green's function bias relative to data at the equator; and (f) Green's function bias relative to data at the 156-m depth. Units are $^\circ\text{C}$.

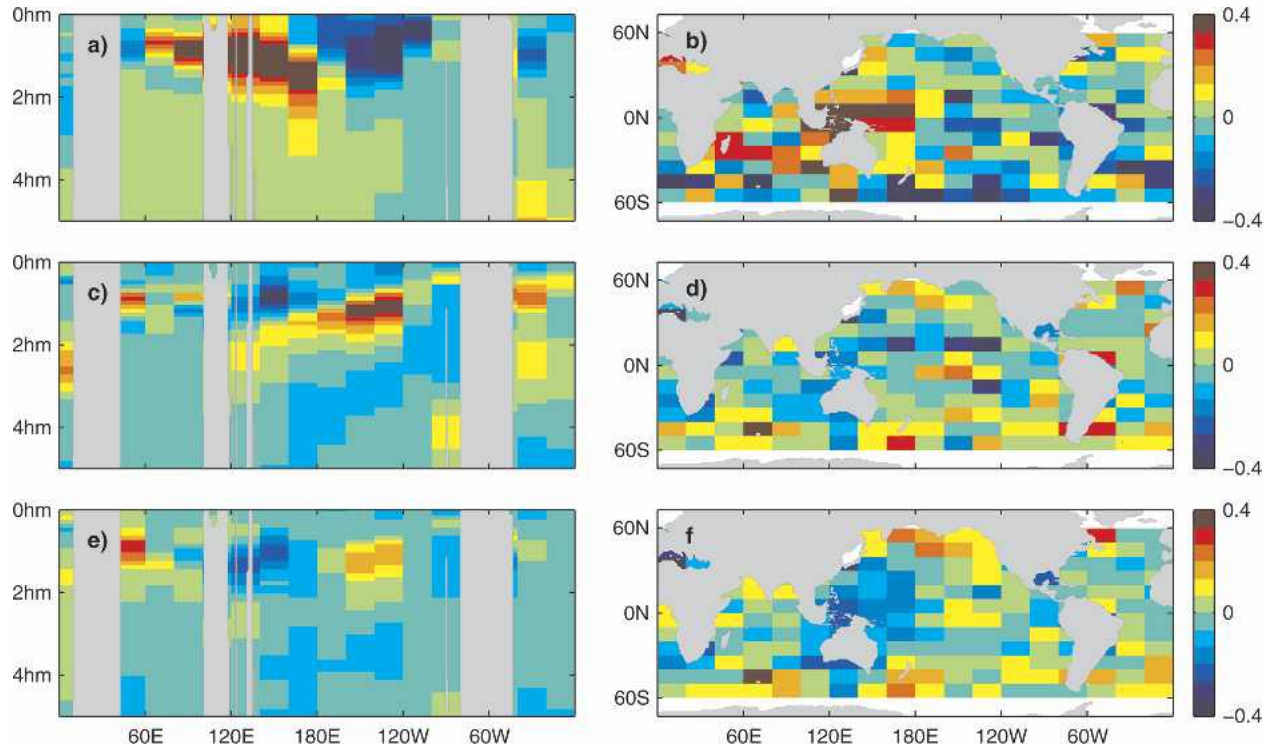


FIG. 14. Potential temperature trend, 1993–2000: (a) Green's function estimate at the equator down to 500-m depth; (b) Green's function estimate at the 156-m depth; (c) smoother drift relative to data at the equator; (d) smoother drift relative to data at the 156-m depth; (e) Green's function drift relative to data at the equator; and (f) Green's function drift relative to data at the 156-m depth. Units are $^{\circ}\text{C yr}^{-1}$.

maintaining model parameterization and boundary condition errors. Therefore these discrepancies can guide future model-parameterization improvements and/or the selection of additional model sensitivity experiments.

g. Drift

Given the large changes in 1991 initial conditions relative to those obtained from model spinup, an important question is whether the bias reduction has

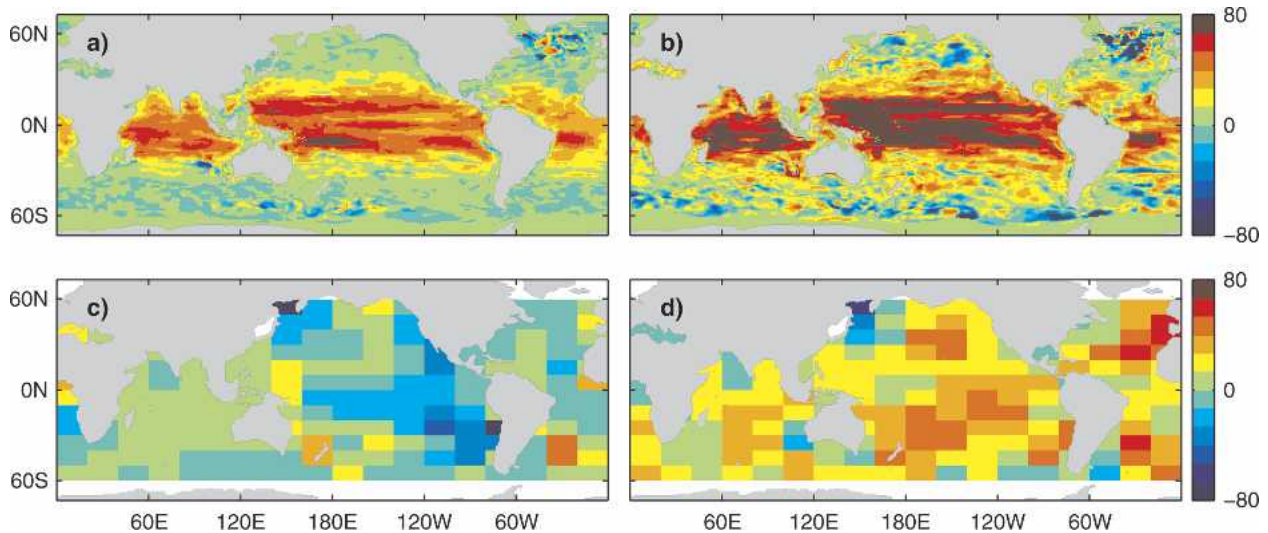


FIG. 15. Percent explained variance of the baseline-data residual for (a) sea surface height variability of the smoother solution, (b) sea surface height variability of the Green's function solution, (c) temperature variability at 156 m of the smoother solution, and (d) temperature variability at 156 m of the Green's function solution.

taken place at the expense of increased drift in the optimized solution. Figure 12b shows that, overall, the Green's function optimization has also reduced the drift of the solution relative to data. The largest drift reduction compared to the prior smoother solution is once again at the base of the equatorial thermocline, as can be seen by comparing Figs. 14c and 14e. There are, however, localized regions where model drift relative to data is larger than that of the baseline and of the smoother integrations, for example, in the northern North Atlantic below 1000-m depth. Again these discrepancies can guide future improvements of the solution, for example, in the representation of high-latitude processes and in the formation of deep water masses.

h. Explained variance

Owing to the improved estimate of the time-mean state and to the combination of solutions, the Green's function optimization also improves model variability of temperature and of sea surface height relative to data compared to both the baseline and to the prior smoother integrations. Figure 12c shows that overall the Green's function solution results in a 10%–30% increase in explained temperature variance compared to the earlier solutions. Explained variance is here defined as one minus the variance of the analysis-data difference divided by the variance of the baseline-data difference:

$$\text{explained variance} = 1 - \frac{\text{var}[G(\boldsymbol{\eta}^a) - \mathbf{y}^o]}{\text{var}[G(\boldsymbol{\eta}^b) - \mathbf{y}^o]} \quad (16)$$

The spatial pattern of the explained variance relative to the baseline integration is shown in Fig. 15 first for sea level and second for temperature at the 156-m depth. The smoother solution, Fig. 15a, already explains a large fraction, up to 50%, of the baseline-data difference for sea level variability. But overall it degrades the temperature variability, as shown in Fig. 15c. Even though the smoother solution has more realistic heaving of the water column than the baseline integration, the resulting temperature variability is degraded compared to observations because the time-mean vertical temperature gradient is inaccurate. By comparison, the Green's function solution improves both the temperature and the sea level variability (Figs. 15b and 15d) even though altimetric data have not been used as constraints.

6. Summary and concluding remarks

The work discussed hereinabove demonstrates that Green's functions provide a simple yet effective method to test and to calibrate GCM parameterizations, to study and to quantify model and data errors, to correct model biases and trends, and to blend estimates from different solutions and data products.

The Green's function method was applied to an

ocean GCM, resulting in substantial improvements of the solution relative to observations as compared to prior estimates: overall model bias and drift are reduced, and there is a 10%–30% increase in explained variance. Within the context of this optimization, the following new estimates for commonly used ocean GCM parameters have been obtained. Background vertical diffusivity is $(15.1 \pm 0.1) \times 10^{-6} \text{ m}^2 \text{ s}^{-2}$. Background vertical viscosity is $(18 \pm 3) \times 10^{-6} \text{ m}^2 \text{ s}^{-2}$. The critical bulk Richardson number, which sets boundary layer depth, is $\text{Ri}_c = 0.354 \pm 0.004$. The threshold gradient Richardson number for shear instability vertical mixing is $\text{Ri}_0 = 0.699 \pm 0.008$. The estimated isopycnal diffusivity coefficient ranges from 550 to 1350 $\text{m}^2 \text{ s}^{-2}$, with the largest values occurring at depth in regions of increased mesoscale eddy activity. Surprisingly, the estimated isopycnal diffusivity exhibits a 5%–35% decrease near the surface. Improved estimates of initial and boundary conditions were also obtained. The above estimates are the backbone of a quasi-operational, global-ocean circulation analysis system whose products are freely available and are being used for a variety of science applications (<http://ecco.jpl.nasa.gov>).

There remain many aspects of the above solution that can be improved, for example, the warm bias in the Indian Ocean at the 200-m depth, the drift of the solution below 1000 m in the northern North Atlantic, and in general the poor representation of high-latitude processes and of deep water mass formation rates. The puzzling estimates of isopycnal diffusivity are also an outstanding research issue; additional control parameters may be required, for example, depth-varying background vertical viscosity and diffusivity to account for increased dissipation rates near rough topography and separate estimates of isopycnal and isopycnal thickness diffusivities. The Green's function approach provides a powerful mechanism for addressing the above questions and for identifying and for reducing residual model-data discrepancies in a physically consistent manner.

Compared to other methods, the key advantages of the Green's function approach are simplicity of implementation, robustness in the presence of nonlinearities, and the explicit computation of the data kernel matrix. While the application of an adjoint model or an approximate smoother require substantial additional model-development and coding efforts, all that is required for applying the Green's function approach is the computation of GCM sensitivity experiments. Furthermore, while the adjoint method requires that the exact tangent linear of the GCM be well behaved, Green's functions provide an approximate linearization, which can be used to reduce the cost function even when the adjoint model is ill behaved, as is the case in the above ocean GCM example. Finally, the explicit computation of the data kernel matrix makes available a vast array of tools from discrete linear inverse theory for deriving and for analyzing the solutions.

The key drawback of the Green's function approach is that computational cost increases linearly with the number of control parameters. Therefore the method is only applicable to situations where a small number of control parameters need to be estimated. Nevertheless the present work demonstrates that a small number of carefully chosen control parameters can result in substantial improvement of the solution. For example, only six control parameters were used in the first test optimization and yet the cost function was reduced by 33%. While in general we do not expect such substantial cost function reduction to be possible for all problems, it is clear that the Green's function approach is an extremely powerful tool in the repertoire of ocean state estimation.

What distinguishes the present work from previous applications of Green's functions to ocean state estimation is the choice of control parameters. Previous applications used model Green's functions to obtain a coarse-scale representation of ocean GCM dynamics, for example, the GCM response to large-scale, geostrophically adjusted density or sea surface height perturbations. The breakthrough here is that rather than using Green's functions to approximate GCM dynamics, Green's functions are instead used to calibrate a small number of key GCM parameters and to blend estimates from existing solutions and data products. This new approach has the advantage of permitting a relatively large impact on the solution from a small number of control variables. Additionally, the representation of GCM dynamics is implicit and exact rather than explicit and approximate.

Work is underway to apply the Green's function approach to a global, eddy-permitting GCM configuration that includes the Arctic Ocean and an interactive sea ice model. The Green's function approach is also being applied to the calibration of an atmospheric GCM and of a coupled ocean-atmosphere climate GCM.

Acknowledgments. This is a contribution of the Consortium for Estimating the Circulation and Climate of the Ocean (ECCO) funded by the National Oceanographic Partnership Program. We are indebted to C. Wunsch for teaching us about inverse methods and for suggesting application of Green's functions to the ocean circulation inverse problem.

REFERENCES

- Barnier, B., L. Siefridt, and P. Marchesiello, 1995: Thermal forcing for a global ocean circulation model using a three-year climatology of ECMWF analysis. *J. Mar. Syst.*, **6**, 363–380.
- Challis, L., and F. Sheard, 2003: The Green of Green functions. *Phys. Today*, **56** (12), 41–46.
- Dickey, J., S. L. Marcus, O. de Viron, and I. Fukumori, 2002: Recent Earth oblateness variations: Unraveling climate and postglacial rebound effects. *Science*, **298**, 1975–1977.
- Fan, S.-M., J. L. Sarmiento, M. Gloor, and S. W. Pacala, 1999: On the use of regularization techniques in the inverse modeling of atmospheric carbon dioxide. *J. Geophys. Res.*, **104** (D17), 21 503–21 512.
- Fukumori, I., 2002: A partitioned Kalman filter and smoother. *Mon. Wea. Rev.*, **130**, 1370–1383.
- , T. Lee, B. Cheng, and D. Menemenlis, 2004: The origin, pathway, and destination of Niño-3 water estimated by a simulated passive tracer and its adjoint. *J. Phys. Oceanogr.*, **34**, 582–604.
- Gent, P. R., and J. C. McWilliams, 1990: Isopycnal mixing in ocean circulation models. *J. Phys. Oceanogr.*, **20**, 150–155.
- Gloor, M., N. Gruber, T. M. C. Hughes, and J. L. Sarmiento, 2001: Estimating net air–sea fluxes from ocean bulk data: Methodology and application to the heat cycle. *Global Biogeochem. Cycles*, **15**, 767–782.
- Gouretski, V. V., and K. P. Koltermann, 2004: WOCE global hydrographic climatology. Berichte des Bundesamtes für Seeschifffahrt und Hydrographie Tech. Rep. 35, 9 pp.
- Gray, S. L., and T. W. N. Haine, 2001: Constraining a North Atlantic Ocean general circulation model with chlorofluorocarbon observations. *J. Phys. Oceanogr.*, **31**, 1157–1181.
- Gross, R. S., I. Fukumori, and D. Menemenlis, 2003: Atmospheric and oceanic excitation of the Earth's wobbles during 1980–2000. *J. Geophys. Res.*, **108**, 2370, doi:10.1029/2002JB002143.
- Heimbach, P., C. Hill, and R. Giering, 2002: Automatic generation of efficient adjoint code for a parallel Navier–Stokes solver. *Lecture Notes in Computer Science*, J. J. Dongarra, P. M. A. Sloot, and C. J. K. Tan, Eds., Springer-Verlag, 1019–1028.
- Holloway, G., 1986: Estimation of oceanic eddy transports from satellite altimetry. *Nature*, **323**, 243–244.
- , 1999: Moments of probable seas: Statistical dynamics of Planet Ocean. *Physica D*, **133**, 199–214.
- Ide, K. P., P. Courtier, M. Ghil, and A. Lorenc, 1997: Unified notation for data assimilation: Operational, sequential and variational. *J. Meteor. Soc. Japan*, **75**, 181–189.
- Kelley, D. E., and K. A. Van Scoy, 1999: A basinwide estimate of vertical mixing in the upper pycnocline: Spreading of bomb tritium in the North Pacific Ocean. *J. Phys. Oceanogr.*, **29**, 1759–1771.
- Kistler, R., and Coauthors, 2001: The NCEP–NCAR 50-year reanalysis: Monthly means CD-ROM and documentation. *Bull. Amer. Meteor. Soc.*, **82**, 247–267.
- Large, W. G., J. C. McWilliams, and S. Doney, 1994: Oceanic vertical mixing: A review and a model with a nonlocal boundary layer parameterization. *Rev. Geophys.*, **32**, 363–403.
- , G. Danabasoglu, S. C. Doney, and J. C. McWilliams, 1997: Sensitivity to surface forcing and boundary layer mixing in a global ocean model: Annual-mean climatology. *J. Phys. Oceanogr.*, **27**, 2418–2447.
- , —, J. C. McWilliams, P. R. Gent, and F. O. Bryan, 2001: Equatorial circulation of a global ocean climate model with anisotropic horizontal viscosity. *J. Phys. Oceanogr.*, **31**, 518–536.
- Lee, T., and I. Fukumori, 2003: Interannual-to-decadal variations of tropical–subtropical exchange in the Pacific Ocean: Boundary versus interior pycnocline transports. *J. Climate*, **16**, 4022–4042.
- Marshall, J., A. Adcroft, C. Hill, L. Perelman, and C. Heisey, 1997: A finite-volume, incompressible Navier–Stokes model for studies of the ocean on parallel computers. *J. Geophys. Res.*, **102** (C3), 5753–5766.
- McKinley, G. A., M. J. Follows, and J. Marshall, 2003: Interannual variability of air–sea O₂ fluxes and the determination of CO₂ sinks using atmospheric O₂/N₂. *Geophys. Res. Lett.*, **30**, 1101, doi:10.1029/2002GL016044.
- Menemenlis, D., and C. Wunsch, 1997: Linearization of an oceanic circulation model for data assimilation and climate studies. *J. Atmos. Oceanic Technol.*, **14**, 1420–1443.

- , and M. Chechelnitsky, 2000: Error estimates for an ocean general circulation model from altimeter and acoustic tomography data. *Mon. Wea. Rev.*, **128**, 763–778.
- Menke, W., 1989: *Geophysical Data Analysis: Discrete Inverse Theory*. International Geophysics Series, Vol. 45, Academic Press, 285 pp.
- Paulson, C. A., and J. J. Simpson, 1977: Irradiance measurements in the upper ocean. *J. Phys. Oceanogr.*, **7**, 952–956.
- Redi, M. H., 1982: Oceanic isopycnal mixing by coordinate rotation. *J. Phys. Oceanogr.*, **12**, 1154–1158.
- Stammer, D., and C. Wunsch, 1996: The determination of the large-scale circulation of the Pacific Ocean from satellite altimetry using model Green's functions. *J. Geophys. Res.*, **101** (C8), 18 409–18 432.
- , and Coauthors, 2003: Volume, heat, and freshwater transports of the global ocean circulation 1993–2000, estimated from a general circulation model constrained by World Ocean Circulation Experiment (WOCE) data. *J. Geophys. Res.*, **108**, 3007, doi:10.1029/2001JC001115.
- , K. Ueyoshi, A. Köhl, W. G. Large, S. A. Josey, and C. Wunsch, 2004: Estimating air–sea fluxes of heat, freshwater, and momentum through global ocean data assimilation. *J. Geophys. Res.*, **109**, C05023, doi:10.1029/2003JC002082.
- Woodruff, S. D., H. F. Diaz, J. D. Elms, and S. J. Worley, 1998: COADS release 2 data and metadata enhancements for improvements of marine surface flux fields. *Phys. Chem. Earth*, **23**, 517–527.
- Wunsch, C., 1996: *The Ocean Circulation Inverse Problem*. Cambridge University Press, 442 pp.